FERROELECTRICS

Ultrafast high-endurance memory based on sliding ferroelectrics

Kenji Yasuda[1,2]†*, Evan Zalys-Geller[1]†, Xirui Wang[1], Daniel Bennett[3], Suraj S. Cheema[4],
Kenji Watanabe[5], Takashi Taniguchi[6], Efthimios Kaxiras[3,7],
Pablo Jarillo-Herrero[1]*, Raymond Ashoori[1]*

The persistence of voltage-switchable collective electronic phenomena down to the atomic scale has extensive implications for area- and energy-efficient electronics, especially in emerging nonvolatile memory technology. We investigate the performance of a ferroelectric field-effect transistor (FeFET) based on sliding ferroelectricity in bilayer boron nitride at room temperature. Sliding ferroelectricity represents a different form of atomically thin two-dimensional (2D) ferroelectrics, characterized by the switching of out-of-plane polarization through interlayer sliding motion. We examined the FeFET device employing monolayer graphene as the channel layer, which demonstrated ultrafast switching speeds on the nanosecond scale and high endurance exceeding 10^{11} switching cycles, comparable to state-of-the-art FeFET devices. These characteristics highlight the potential of 2D sliding ferroelectrics for inspiring next-generation nonvolatile memory technology.

The quest for a high-speed, voltage-driven, nonvolatile memory with high endurance in low-power and reliable operation remains a longstanding challenge in addressing the explosion of data in modern technology. A promising candidate technology for energy-efficient nonvolatile memory is the ferroelectric field-effect transistor (FeFET), in which the electrical conductance and threshold voltage of the channel layer is controlled by switching the electric polarization of an adjacent ferroelectric layer by an applied electric field. Despite intensive efforts to integrate conventional ferroelectrics into nonvolatile memory technology, challenges such as endurance and thickness scaling remain, underscoring the need for novel ferroelectric materials. Discovery of certain ferroelectric materials such as fluorite-structure HfO_2-ZrO_2 (1) and wurtzite-structure AlN-ScN (2) has triggered a resurgence of interest in FeFET memory. These three-dimensional (3D) materials stand out because of their robust ferroelectric properties even in the ultra-thin limit (3, 4), which opens avenues for the development of energy-efficient and scalable FeFETs (5). Another emerging category of ultrathin ferroelectrics is 2D van der Waals materials. The absence of dangling bonds and conventional ferroelectric size effects in these materials enables ferroelectricity down to a thickness of a few layers (6, 7), offering promising pathways for next-generation device applications.

2D materials, because of their stacking degrees of freedom, also offer a different pathway to ferroelectricity in comparison to their 3D ferroelectric counterparts, which can potentially improve nonvolatile memory operation. Recently, a type of 2D ferroelectricity known as sliding ferroelectrics was discovered, in which the polarization is switched through an interlayer sliding motion (8). This sliding motion is enabled by the weak van der Waals nature of the interlayer bonding of layered 2D materials. Sliding ferroelectricity appears in exfoliated 2D materials from bulk crystals such as WTe_2 and $MoTe_2$ (9, 10), as well as in artificially stacked van der Waals heterostructures of 2D materials. For example, boron nitride (BN) (11–13) and semiconducting transition metal dichalcogenides (TMDs), such as MoS_2 (14–16), can be made ferroelectric by altering the stacking orders from their natural configurations. This synthetic approach to ferroelectricity has expanded the category of 2D ferroelectrics to a much broader range of 2D materials with exceptional physical properties.

We show a schematic illustration of commonly used bulk hexagonal BN (hBN) crystals (Fig. 1A). Each layer consists of a honeycomb lattice made of boron and nitrogen atoms, stacked in an AA' configuration, meaning that one layer of BN is rotated 180 degrees with respect to the other. Because of this 180-degree rotated stacking order, bulk hBN is centrosymmetric and nonferroelectric. Meanwhile, using the van der Waals assembly technique established for 2D materials, artificial creation of a new stacking order is possible in which two layers of BN are stacked in parallel, a 0-degree orientation. In this configuration, BN adopts either an AB or BA stacking order (Fig. 1B), which are energetically degenerate. As the space group is rhombohedral in these stacking orders, parallel-stacked BN is also called rhombohedral BN. Because of the vertical alignment of boron and nitrogen atoms, interlayer charge transfer occurs from the nitrogen atom to the boron atom, creating a finite electric dipole moment and macroscopic electrical polarization. For the AB stacking configurations, the boron atom is located above the nitrogen atom whereas in the BA stacking configuration the nitrogen atom is located above the boron atom. Accordingly, these two different stacking orders lead to out-of-plane electrical polarization in the upward and downward directions, respectively, as can be seen from mirror symmetry breaking of differential charge distribution. Previous experimental work demonstrated that these AB and BA stackings transform between each other by applying a vertical electric field (11, 12). The switching occurs through the interlayer sliding motion, namely, by shifting one layer by 1/3 of the unit cell. The unconventional coupling between in-plane sliding motion and out-of-plane polarization switching is specific to these materials and this ferroelectricity is referred to as sliding ferroelectricity.

Parallel-stacked bilayer BN, consisting of two atomic sheets, exhibits robust sliding ferroelectricity at room temperature despite its miniscule thickness of 0.67 nm. This property positions it as a promising candidate for the development of energy-efficient nanoscale FeFETs, as the required voltage for switching scales with the thickness of the material. Notably, BN serves as an exceptional environmental protection layer for other 2D materials such as graphene and TMDs, leading to higher mobility and an enhanced on/off ratio. Consequently, investigating the ferroelectric characteristics of BN is of critical importance in advancing next-generation device applications based on 2D materials and van der Waals heterostructures (17). We constructed a van der Waals heterostructure–based FeFET, utilizing monolayer graphene as the channel layer, to evaluate the switching speed and endurance of ferroelectric BN. We discovered that it exhibits nanosecond scale ferroelectric switching speed and has a high endurance of 10^{11} switching cycles, comparable to the best values reported in HfO_2-based FeFETs (18–20).

Basic characterization

For our device structure we sandwiched a monolayer graphene between top and bottom bulk hBN (Fig. 1C). These hBN layers possess conventional AA' stacking and are nonferroelectric, and we use them as gate dielectrics. We inserted a parallel-stacked bilayer BN layer that exhibits sliding ferroelectricity. Depending on the out-of-plane polarization direction of the

[1]Department of Physics, Massachusetts Institute of Technology, Cambridge, MA 02138, USA. [2]School of Applied and Engineering Physics, Cornell University, Ithaca, NY 14850, USA. [3]John A. Paulson School of Engineering and Applied Sciences, Harvard University, Cambridge, MA 02138, USA. [4]Research Laboratory of Electronics, MA Institute of Technology, Cambridge, MA, USA. [5]Research Center for Electronic and Optical Materials, National Institute for Materials Science, Tsukuba 305-0044, Japan. [6]Research Center for Materials Nanoarchitectonics, National Institute for Materials Science, Tsukuba 305-0044, Japan. [7]Department of Physics, Harvard University, Cambridge, MA 02138, USA.
*Corresponding author. Email: kenji.yasuda@cornell.edu (K.Y.); pjarillo@mit.edu (P.J.H.); ashoori@mit.edu (R.A.)
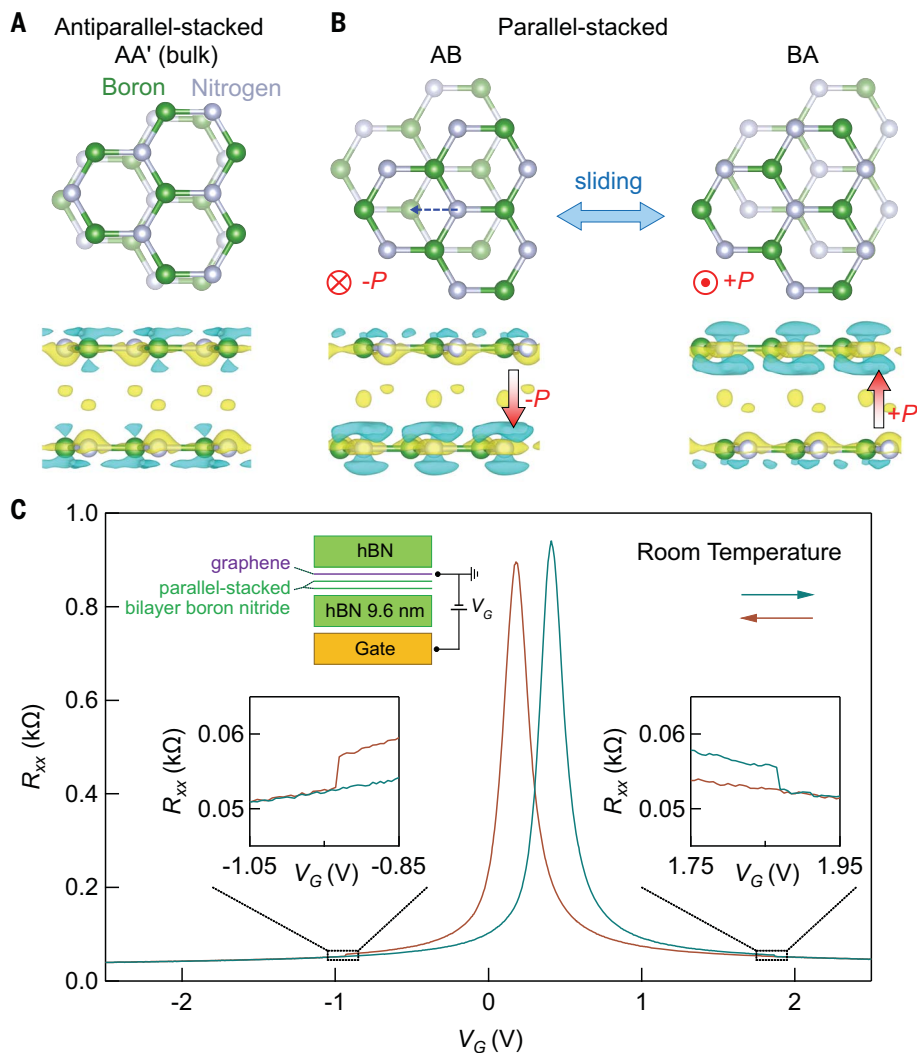†These authors contributed equally to this work.

Fig. 1. Basic characteristics of a ferroelectric field-effect transistor based on sliding ferroelectrics.
(**A**) Schematic of the crystal structure of antiparallel-stacked bilayer boron nitride with AA' stacking. Nitrogen and boron atoms are displayed in silver and green, respectively. The bottom panel shows the differential charge distribution mapping. The yellow and blue region corresponds to the increased negative and positive charge as compared to a monolayer, respectively. The figures are drawn using VESTA (*44*). (**B**) Schematic of the crystal structures of parallel-stacked bilayer boron nitride. AB and BA stacking creates out-of-plane ferroelectric polarization in opposite directions, which can be switched by the interlayer sliding motion, denoted by the dotted blue line. (**C**) Resistance of monolayer graphene R_{xx} as a function of the gate voltage V_G. The green and brown curves correspond to forward and backward scans, respectively. The inset shows the schematic of the side view of the ferroelectric field-effect transistor and enlarged view at the ferroelectric switching voltages.

parallel-stacked bilayer BN, either negative or positive charge is injected into the graphene monolayer. This allows us to determine the ferroelectric polarization direction by measuring the resistance of the graphene. We conducted all measurements under a vacuum at room temperature.

Considering the resistance of the graphene as a function of the gate voltage V_G (Fig. 1D), we observed a peak in resistance, corresponding to the charge neutrality condition of graphene. Unlike conventional graphene FET devices, however, we observe hysteresis as a function of gate voltage. The green and brown curves are forward and backward scans, respectively. We found a prominent hysteresis depending on the scanning direction of the gate voltage. As we applied the voltage between graphene and the gate, the electric field is applied to the parallel-stacked bilayer BN, which results in the switching of the out-of-plane polarization. Furthermore, the resistance exhibited abrupt changes around V_G = 1.85 V and V_G = −0.9 V, which stems from the ferroelectric polarization switching between down-to-up and up-to-down, respectively.

Ultrafast switching of sliding ferroelectrics

We explored the pulse width dependence of the switching voltage. We first initialized the polarization to the up state by applying V_G = 2.5 V. We then applied a voltage pulse with varying lengths and widths. After this we measured the resistance of the graphene sensing layer at V_G = 0.21 V to check whether polarization had switched (Fig. 2A, upper portion). V_G = 0.21 V is the charge neutrality condition of the up-polarization state. Therefore, the red (blue) color in the color plot indicates up (down) polarization. We also performed a similar procedure by initializing the polarization to down by applying V_G = −2.5 V and applying a pulse with varying lengths and widths (Fig. 2B). We investigated switching kinetics over 10 orders of magnitude in time, from 1 ns to 10 s for up to down polarization switching and from 1 ns to 5 s for down to up polarization switching. The critical voltage for polarization switching increases as the pulse width decreases (Fig. 2), in accordance with classic models of ferroelectric switching kinetics (*21–23*). Crucially, we can switch the device's polarization switching with a pulse width as short as 1 ns for both up-to-down and down-to-up polarization switching. The switching speed of 1 ns is only limited by our instrumentation and by the design of the device, which is not optimized for RF signals. Despite these limitations, our device's measured performance is comparable to that of state-of-the-art HfO$_2$-based FeFET devices (*24*).

The ferroelectric switching occurs through ferroelectric domain wall motion. The coercive field expected for coherent homogeneous switching is 7.8 V/nm (*8, 25*). Meanwhile, the experimentally obtained coercive field is 0.3 V/nm, more than 20 times smaller than the estimated value for coherent switching. This discrepancy tells us that switching occurs through domain nucleation and growth rather than uniform switching of the entire device. This observation is consistent with the real space imaging of electric-field–induced domain wall motion of sliding ferroelectrics based on scanning probe (*12, 14, 26*) and electron microscopy techniques (*15, 16*). Assuming that switching happens through the motion of a single domain wall, we calculate the domain wall speed to be as high as 1000 m/s by dividing the device size of around 1 μm by the pulse width of 1 ns. This ultrafast domain wall speed is consistent with theoretical predictions (*27*) and is much faster than the previously reported speed of 300 μm/s in sliding ferroelectric WSe$_2$ (*16*). The shorter pulse we applied enabled the observation of the ultrafast domain wall motion in our system, which could be useful for domain wall–based nanoelectronics (*28*).

The domain wall speed approaches the speed of shear phonon modes of around 18000 m/s (*29*), which should be the physical limitation of the domain wall motion. Investigating how
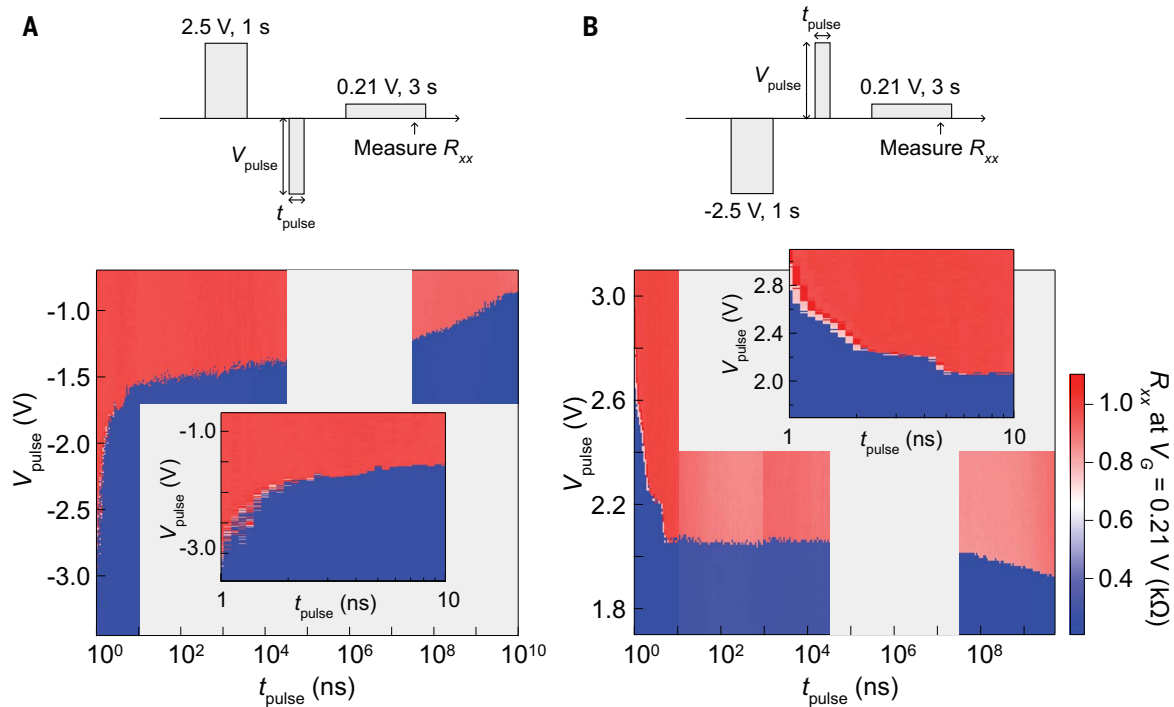
Fig. 2. Pulse width dependence of switching voltage. (A) (Top) Illustration of the measurement procedure. (Bottom) Resistance of monolayer graphene R_{xx} measured at V_G = 0.21 V after the application of a negative voltage pulse of V_{pulse} and t_{pulse}. The inset shows the enlarged view from 1 ns to 10 ns. We could not apply a well-defined pulse between 30 ms and 30 μs due to significant distortion of the pulse shape because of the bias tee placed near the sample (fig. S1). This region is shaded in gray. **(B)** Same as (A) for the positive voltage pulses.

domain wall dynamics change when driven close to phonon speeds would be interesting as it might involve relativistic motion, as demonstrated for ferromagnetic domain wall motion (30). Real-space imaging will be invaluable for understanding the dynamics of ferroelectric switching in sliding ferroelectricity from both fundamental and application perspectives (11, 12, 14–16, 26, 31). Going further, coherent and uniform switching of the entire layer may even be possible with ultrafast optical light on a picosecond-timescale (32–34).

High endurance of sliding ferroelectrics

We measured the endurance of ferroelectric switching, starting by applying single pulses with a width of 100 ns and a height of V_{pulse} = 3.1 V and V_{pulse} = −3.1 V repeatedly up to $1.11{\times}10^4$ switching cycles. Next, we applied a square wave with a peak height of ±3.1 V with a frequency of up to 10^7 Hz for variable durations of time. After application of the square wave we applied two voltage pulses of V_{pulse} = 3.1 V and V_{pulse} = −3.1 V each with the width of 100 ns and measured the graphene's resistance at V_G = 0.15 V to confirm that the ferroelectric property was not degraded (Fig. 3). V_G = 0.15 V is the charge neutrality condition of the up-polarization state, which drifted slightly from that in Fig. 2. The switching properties of ferroelectric BN remain almost unchanged over 10^{11} switching cycles (Fig. 3), as seen from the

polarization switching by the voltage pulses. We further verified that the magnitude of polarization and the coercive field remains almost unchanged after the switching cycle (fig. S2).

The fatigueless switching we observed in our FeFET devices, exceeding 10^{11} cycles without altering the ferroelectric characteristics, is comparable to the best-performing FeFET devices reported in HfO_2 (18–20). High endurance in ferroelectric BN was achieved without any optimization of the sample or device structure. The high endurance in HfO_2, by contrast, required over 10 years of optimization of the interfacial layers (1, 5, 18–20). The high endurance of our devices underscores the inherent robustness of polarization switching in sliding ferroelectrics. The degradation of conventional FeFETs over extensive switching typically originates from the creation of defects at the interfacial layer between the ferroelectrics and the channel layer. These defects lead to premature breakdown of the interfacial layer and a decrease in polarization and memory window in the ferroelectric layer (35). Unlike conventional switching mechanisms that involve switching ionic dipoles, sliding ferroelectrics rely on the in-plane sliding motion between the layers bonded by physical van der Waals force. We speculate that these characteristics prevent the creation of defects at the interface or that any defects created in each layer do not

affect the sliding motion, contributing to the high endurance of sliding ferroelectrics.

Conclusions

The combination of ultrafast switching and high endurance, together with subnanometer thickness, sub-3.3-V operation required for embedded memory, and retention exceeding one month (11), underscore the potential of sliding ferroelectrics in nonvolatile memory technology (see table S1). At the same time, there are several critical challenges that remain to be addressed for practical applications. One major challenge is achieving wafer-scale synthesis of sliding ferroelectrics, which could be realized by advancing existing growth techniques of rhombohedral BN, such as chemical vapor deposition and sputtering (36–40). Another challenge is improving the on/off ratio. The inherently small polarization in sliding ferroelectrics results in limited on/off ratio in the FeFET geometry. This challenge can be addressed by adopting a device geometry that relies not on the absolute magnitude of polarization but rather on the band alignment between the layers. For example, a sliding ferroelectric MoS_2 device has recently achieved on/off ratios that span six orders of magnitude in a ferroelectric semiconductor field-effect transistor geometry that utilizes the ferroelectric semiconductor itself as the channel layer (41). Although technological integration challenges remain, 2D-based
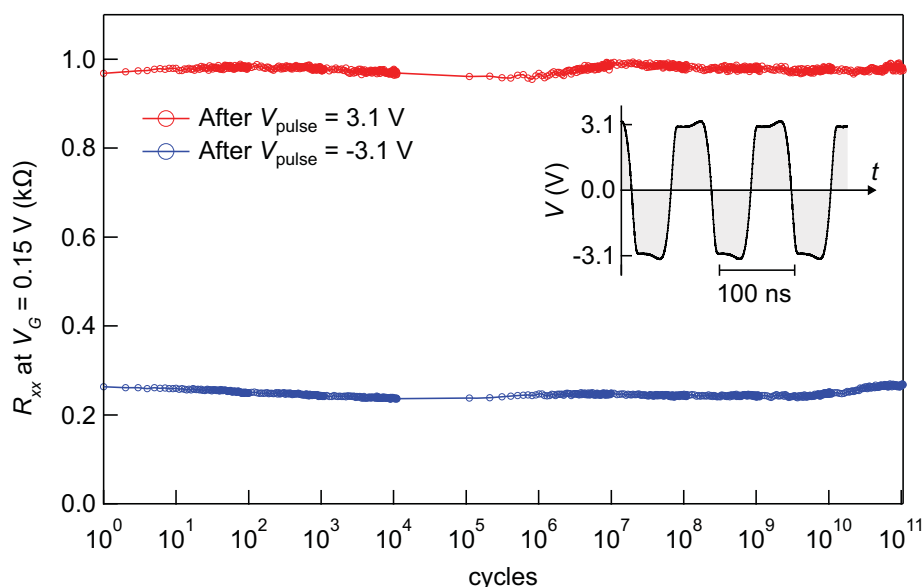
Fig. 3. Endurance of sliding ferroelectrics against switching cycles. Resistance of monolayer graphene R_{xx} measured at $V_G = 0.15$ V after the sets of voltage pulse or ac square voltage, followed by the application of voltage pulses of $V_{pulse} = -3.1$ V and $V_{pulse} = 3.1$ V with pulse width of 100 ns. The inset shows the shape of the ac square voltage with 10^7 Hz measured by an oscilloscope.

FeFET memory technology is currently being pursued by semiconductor foundries (*42*). We anticipate that our research demonstrating superior nonvolatile memory performance derived from a novel mechanism of ferroelectric switching will spur further research into nonvolatile memory technology based on sliding ferroelectrics.

REFERENCES AND NOTES

1. T. S. Böscke, J. Müller, D. Bräuhaus, U. Schröder, U. Böttger, *Appl. Phys. Lett.* **99**, 102903 (2011).
2. K. H. Kim, I. Karpov, R. H. Olsson III, D. Jariwala, *Nat. Nanotechnol.* **18**, 422–441 (2023).
3. H.-J. Lee *et al*., *Science* **369**, 1343–1347 (2020).
4. S. S. Cheema *et al*., *Science* **376**, 648–652 (2022).
5. U. Schroeder, M. H. Park, T. Mikolajick, C. S. Hwang, *Nat. Rev. Mater.* **7**, 653–669 (2022).
6. M. Wu, J. Li, *Proc. Natl. Acad. Sci. U.S.A.* **118**, 50 (2021).
7. D. Zhang, P. Schoenherr, P. Sharma, J. Seidel, *Nat. Rev. Mater.* **8**, 25–40 (2023).
8. L. Li, M. Wu, *ACS Nano* **11**, 6382–6388 (2017).
9. Z. Fei *et al*., *Nature* **560**, 336–339 (2018).
10. A. Jindal *et al*., *Nature* **613**, 48–52 (2023).
11. K. Yasuda, X. Wang, K. Watanabe, T. Taniguchi, P. Jarillo-Herrero, *Science* **372**, 1458–1462 (2021).
12. M. Vizner Stern *et al*., *Science* **372**, 1462–1466 (2021).
13. C. R. Woods *et al*., *Nat. Commun.* **12**, 347 (2021).
14. X. Wang *et al*., *Nat. Nanotechnol.* **17**, 367–371 (2022).
15. A. Weston *et al*., *Nat. Nanotechnol.* **17**, 390–395 (2022).
16. K. Ko *et al*., *Nat. Mater.* **22**, 992–998 (2023).
17. C. Liu *et al*., *Nat. Nanotechnol.* **15**, 545–557 (2020).
18. S. De *et al*., in *2021 Symposium on VLSI Technology* (IEEE, 2021), vol. 1, pp. 1–2.
19. A. J. Tan *et al*., *IEEE Electron Device Lett.* **42**, 994–997 (2021).
20. M. C. Nguyen *et al*., *IEEE Electron Device Lett.* **42**, 1295–1298 (2021).
21. Y. Ishibashi, Y. Takagi, *J. Phys. Soc. Jpn.* **31**, 506–510 (1971).
22. M. Avrami, *J. Chem. Phys.* **7**, 1103–1112 (1939).
23. A. K. Tagantsev, I. Stolichnov, N. Setter, J. S. Cross, M. Tsukada, *Phys. Rev. B* **66**, 214109 (2002).
24. M. M. Dahan *et al*., *Nano Lett.* **23**, 1395–1400 (2023).
25. Materials and methods are available as supplementary materials.
26. M. Lv *et al*., *Adv. Mater.* **34**, e2203990 (2022).
27. R. He *et al*., *Acta Mater.* **262**, 119416 (2024).
28. D. Meier, S. M. Selbach, *Nat. Rev. Mater.* **7**, 157–173 (2022).
29. R. J. Jiménez-Riobóo *et al*., *Appl. Phys. Lett.* **112**, 051905 (2018).
30. L. Caretta *et al*., *Science* **370**, 1438–1442 (2020).
31. C. R. Woods *et al*., *Nat. Commun.* **12**, 347 (2021).
32. J. Park, I. W. Yeu, G. Han, C. S. Hwang, J. H. Choi, *Sci. Rep.* **9**, 14919 (2019).
33. H. Xu, J. Zhou, Y. Li, R. Jaramillo, J. Li, *Nano Res.* **12**, 2634–2639 (2019).
34. R. Mankowsky, A. von Hoegen, M. Först, A. Cavalleri, *Phys. Rev. Lett.* **118**, 197601 (2017).
35. E. Yurchuk *et al*., in *2014 IEEE International Reliability Physics Symposium* (IEEE, 2014).
36. M. Chubarov, H. Pedersen, H. Högberg, J. Jensen, A. Henry, *Cryst. Growth Des.* **12**, 3215–3220 (2012).
37. P. Sutter, J. Lahiri, P. Zahl, B. Wang, E. Sutter, *Nano Lett.* **13**, 276–281 (2013).
38. S. M. Gilbert *et al*., *2D Mater* **6**, 021006 (2019).
39. L. Souqui, J. Palisaitis, N. Ghafoor, H. Pedersen, H. Högberg, *J. Vac. Sci. Technol. A* **39**, 013405 (2021).
40. L. Wang *et al*., *Nature* **629**, 74–79 (2024).
41. T. H. Yang *et al*., *Nat. Electron.* **7**, 29–38 (2023).
42. T.-E. Lee *et al*., *2023 International Electron Devices Meeting* (IEEE, 2024).
43. V. Koshkina *et al*., Data from: Integrated species distribution models: combining presence-background data and site-occupany data with imperfect detection, Dryad (2018); https://datadryad.org/stash/dataset/doi:10.5061/dryad.1jwstqk3c.
44. K. Momma, F. Izumi, *J. Appl. Cryst.* **44**, 1272–1276 (2011).